

Adjustable Bolted Steel Plate Connection: Measured Behavior of Bolts during Field Installation and Numerical Parametric Investigation

Evan J. Gerbo, S.M.ASCE¹; Ashley P. Thrall, A.M.ASCE²; Theodore P. Zoli, P.E., M.ASCE³

ABSTRACT

This paper presents an experimental investigation of bolt behavior in adjustable bolted steel plate connections during field installation and a numerical finite element (FE) parametric investigation of the impact of (1) bolt diameter, (2) plate thickness, and (3) member flange thickness on the strains induced in the plates and bolts during field installation. The adjustable connection consists of prefabricated cold bent plates which are further bent during field installation (via bolt tightening) to form moment-resisting joints between steel members. The connection is adjustable, as the bolt tightening field installation process changes the connection angle in-situ to accommodate additional angles or manufacturing and erection tolerances. This paper presents the residual bolt surface strains, measured using the full-field photographic technique Digital Image Correlation, providing unprecedented information on the behavior of high-strength bolts. An FE modeling approach for predicting strains in the plates and bolts is developed and validated against measured data. Parametric studies are then performed using the validated FE models with varying bolt diameter, plate thickness, and member flange thickness. Research results are relevant to any misaligned (i.e., non-flush) bolted connections, offering insight into strains from force fitting.

Author Keywords: Bolted steel connection; Cold bending; Prefabrication; Rapid Erection;

INTRODUCTION

An adjustable bolted steel plate connection [Figure 1, Gerbo et al. (2018)] is a new approach

¹PhD Candidate, Kinetic Structures Laboratory, Department of Civil & Environmental Engineering & Earth Sciences, University of Notre Dame, Notre Dame, IN 46556. E-mail: egerbo@nd.edu

²Myron and Rosemary Noble Associate Professor of Structural Engineering, Kinetic Structures Laboratory, Department of Civil & Environmental Engineering & Earth Sciences, University of Notre Dame, Notre Dame, IN 46556. (corresponding author) E-mail: athrall@nd.edu

³National Bridge Chief Engineer, HNTB Corp., Empire State Building, 350 5th Ave., 57th Floor, New York, NY 10118. E-mail: tzoli@hntb.com

22 for the rapid erection of steel buildings and bridges. The slip-critical splice connection consists of
23 prefabricated cold bent plates (prebent via a press brake), constituting a kit-of-parts. The plates
24 are further bent in the field via bolt tightening until an adaptation of the turn-of-nut criteria are
25 met [i.e., after plies are brought into firm contact with one another, additional turns are performed
26 consistent with those recommended by the turn-of-nut criteria (Research Council on Structural
27 Connections, 2014)] to join flanges of angled wide flange members. Flanges (member, hereafter)
28 are connected by three of these bent splice plates (plates, hereafter): a top plate and two narrower
29 bottom plates straddling the web (Figure 1C). Webs are connected by straight splices in dou-
30 ble shear. By connecting the flanges and webs independently, a moment-resisting connection is
31 achieved. The connection is adjustable, as the bolt tightening field installation process enables the
32 kit-of-parts of bent plates to join a variety of angles or accommodate manufacturing and erection
33 tolerances.

34 The authors have previously (1) experimentally and numerically investigated the surface strains
35 induced in the plates due to prefabrication (Gerbo et al., 2016) and (2) experimentally investigated
36 the plate surface strains due to field installation (Gerbo et al., 2018). This prior investigation found
37 that (1) differences in connection ply angles at or below 2.5° keep plate field installation strains
38 within reasonable bounds (0.01 mm/mm), (2) a criss-cross bolt tightening pattern with one turn of
39 each bolt per increment was preferred for evenly distributed plate strains, and (3) the maximum
40 field installation strain induced in the plates is primarily dependent on differences in connection
41 ply angles (Gerbo et al., 2018). This prior research has focused only on the behavior of the plates.

42 There is no existing research on the behavior of the bolts in the adjustable bolted steel plate con-
43 nection, specifically, or for the more general case of misaligned (i.e., non-flush plies) bolted splice
44 connections. While there is a great deal of research on bolted steel connections (e.g., Kulak et al.
45 2001, Douty and McGuire 1965, Munse et al. 1959, Rajasekharan et al. 1974, Chesson and Munse
46 1965, AASHTO 2014), this existing research considers the connection plies to have no more than
47 $1/20.0$ (2.86°) relative slope between plies at the initiation of tightening. This research investigates
48 connections with greater relative slopes between plies [i.e., up to $1/7.60$ (7.50°)]. While the focus

49 is on the adjustable bolted steel plate connection, the results are relevant for misaligned bolted
50 splice connections, generally. Misaligned bolted splice connections often occur during construc-
51 tion and are handled by force fitting. The effects of this force fitting are not well understood or
52 controlled. During bolt tightening, of either the adjustable bolted steel plate connection or mis-
53 aligned connections, the high-strength bolts are subjected to bending as they plastically deform
54 the plies of the connection into firm contact with each other, in addition to the axial pre-tension
55 typical of slip-critical connections. It is critical to investigate both the bending and axial strains
56 induced in the bolts during field installation to ultimately understand the impact of installation on
57 the connection's behavior.

58 **OBJECTIVES AND SCOPE**

59 The objectives of this paper are to (1) experimentally investigate strains induced in bolts of
60 adjustable bolted steel plate connections during field installation and (2) numerically investigate
61 the impact of bolt diameter, plate thickness, and member flange thickness on the plate and bolt
62 strains induced during field installation. The full-field, residual surface strains of bolts in 14 ex-
63 perimentally tested scenarios (Table 1) are measured using three-dimensional (3D) digital image
64 correlation (DIC) to investigate the effect of the bolt-tightening procedure, amount and direction of
65 bending, and plate angle. A finite element (FE) numerical modeling approach for the field installa-
66 tion process is developed and validated by comparing these measured residual bolt strains with FE
67 predictions. The measured plate strains presented in Gerbo et al. (2018) are also compared with FE
68 predictions. A parametric study, using the validated FE modeling approach, is then performed to
69 investigate the effect of bolt diameter, plate thickness, and member flange thickness on the resid-
70 ual bolt strains due to field installation and plate strains induced during field installation and the
71 cumulative fabrication process (including also strains from prefabrication via press brake). This
72 research provides unprecedented information on the behavior of high-strength bolts and the results
73 are relevant to any misaligned (i.e., non-flush) bolted connections.

74 **EXPERIMENTAL PROGRAM**

75 A total of 14 scenarios were experimentally tested to investigate the effect of (1) bolt-tightening

76 procedure, (2) amount and direction of plate bending during field installation, and (3) plate angle
77 on the field installation strains induced in the bolts [Table 1, Figure 1E and 1F, Gerbo et al. (2018)].

78 The geometric parameters of the tested connection (Figure 2A and 2B) were selected in Gerbo
79 et al. (2018) for greatest versatility with respect to manufacturing or erection tolerances and mem-
80 ber dimensions. The kit-of-parts of bent plates is intentionally comprised of as few a number of
81 unique parts as possible. The angle of the top plates (γ) is chosen to be equal to that of the bottom
82 plates (β), with values of 5° , 10° , and 15° as well as a non-bent 0° option. Similarly, the radius of
83 curvature of the top plate (r_t) is equal to that of the bottom plate (r_b), with a magnitude of 102 mm
84 (4 in.). The length of the top plate (l_1) is the same as the bottom plate (l_2). These plates will join
85 members at varying angles (α), with a difference in ply angles, $\delta = \alpha - \gamma$.

86 The field installation was tested by connecting the top flanges of ASTM A992 (ASTM, 2015)
87 W10x88 wide flange sections with 3 ASTM A36 (ASTM, 2014b) plates: 1 top plate and 2 bottom
88 plates. Note that the ends of the W10x88 wide flange sections were not mitered in the experimental
89 program for simplicity, but would be in practice as envisioned in Figure 1A - 1C. The thickness
90 of the plates (t_s) were chosen to be approximately half the thickness of the member flange (t_m),
91 typical of bolted splice connections in double shear. 165 mm (6.5 in.) long ASTM A325 (ASTM,
92 2014a) bolts with 19.1 mm (0.750 in.) diameter (d_b) were used in all tested scenarios. Two, 31.8
93 mm (1.25 in.) long hardened stainless steel spacers were used to facilitate experimental testing, as
94 well as 5 ASTM F436 (ASTM, 2018) washers (1 washer was placed between the plates and each
95 spacer, as well as another washer between the bolt head and spacer, and 2 washers were placed
96 between the nut and spacer). Plate hole diameters (d_{ph}) were oversized bolt holes [$d_{ph} = 23.8$ mm
97 (0.9375 in.)] with end distances (l_3) set to 76.2 mm (3.00 in.) and member hole diameters (d_{mh})
98 were long-slotted holes [$d_{mh} = 47.6$ mm (1.875 in.)] based on geometric studies performed in
99 Gerbo et al. (2018). An additional control scenario using flush plies (i.e., plies are flat and parallel,
100 with only two plates and one bolt) was also tested (Scenario 14).

101 The test procedure involved first loosely assembling the plates and bolt assemblies on the re-
102 action frame (Figure 1E) and adjusting the bolt assemblies to have the same nut position [within

103 0.508 mm (0.0200 in.)). A controlled tightening procedure, using the torque wrench and tools
104 shown in Figure 1F, was then performed until the plies of the connection were in full contact. The
105 bolt was held in position during tightening of the nut in specified increments (Table 1) until con-
106 tact is achieved at each bolting location [contact was determined by attempting to fit a 0.254 mm
107 (0.0100 in.) shim between the plate and member]. After contact was achieved at all bolting loca-
108 tions, a final 1 turn of each bolt was completed to satisfy the adaptation of the turn-of-nut criteria
109 (Research Council on Structural Connections, 2014). Match marks were made on the bolt head
110 and nut in the initial untightened position. These marks were then used to track the total number
111 of turns at each nut throughout tightening.

112 Residual strains of the bolts were measured using DIC. DIC is a noncontact photographic
113 technique that uses photogrammetric triangulation and pattern recognition to calculate full-field
114 surface strains. To facilitate pattern recognition, a random pattern was etched onto the shank of
115 the bolts using CerMark LMM-6000 Metal Laser Marking Spray (Ferro, 2016) and a laser cutter
116 (Universal Laser Cutter, VLS 6.60, 50W laser). The DIC photographs were taken with 6 separate
117 readings per bolt prior to testing and after testing (i.e., after connection disassembly) to calculate
118 the residual strains from field installation. The data was assembled to form 3D surface strain
119 maps that were unwrapped to form a flat image (e.g., Figure 3, positive indicates tension and
120 negative indicates compression throughout the paper). The unwrapping used a series of fitted polar
121 coordinate systems, along the bolt length, to minimize distortion in the final unwrapped image.
122 The coordinate system origin is at the side of the bolt facing away from the connection centerline,
123 at mid-height of the bolt (Figure 3). To quantify noise, several DIC measurements were taken prior
124 to testing when the bolts were under no load. The standard deviation of these measurements yields
125 noise levels on the order of 0.00052 mm/mm. This represents 0.8% of the peak strains observed in
126 this study (approximately 0.06 mm/mm). There was loss of DIC data in locations that experience
127 surface abrasion, which generally align with locations of compression.

128 Gerbo et al. (2018) reported the surface plate strains from these tests, also measured using DIC.
129 Throughout the paper, the discussed plate strains are those at full tightening. Reported bolt strains

130 are residual strains (i.e., measured after the connection has been disassembled).

131 **NUMERICAL MODELING**

132 3D FE models of field installation were built in ABAQUS Standard (ABAQUS, 2014). Nonlin-
133 ear material properties were modeled using an isotropic hardening model based on measured true
134 stress-strain relationships for the plate [A36, ASTM (2014b)] and bolt [A325, ASTM (2014a)]
135 steels [see Gerbo et al. (2018)]. Nonlinear geometry was considered. C3D8R elements were used,
136 with a typical mesh size of 1.59 mm (0.0625 in.) in the plates, 3.17 mm (0.125 in.) in the member,
137 and 1.27 mm (0.0500 in.) in the bolts.

138 The models use symmetry along two planes to limit computational expense. To enforce sym-
139 metry, translation restraints in the z direction are applied to the member and plate surfaces cut by
140 the xy plane, and translation restraints in the x direction are applied to the plate surfaces cut by
141 the yz plane (Figure 4A). Only a portion of the member is modeled: half of the web and 305 mm
142 (12.0 in.) of the member length. Boundary conditions provide restraint against all translation at
143 the cut faces of the member to simulate a rigid reaction frame (Figure 4B). Stability in the vertical
144 (y) direction is maintained through the contact interactions between the member and plates, and
145 between the plates and bolt assembly. The bolt assembly has no boundary conditions, with stabil-
146 ity derived from contact interactions. Tangential behavior of the contact interactions is modeled
147 with a penalty friction formulation (with the exception of the bolt shank to nut interaction which
148 is considered frictionless as part of a simplification related to thread interaction), and assumed to
149 have frictional coefficients of 0.33, as recommended for steel on steel faying surfaces (Kulak et al.
150 2001 and AASHTO 2014). The normal behavior of the contact interactions is modeled with a
151 linear stiffness formulation [spring constant of 27.1 GPa/mm (100,000 ksi/in)] to allow for conver-
152 gence. To aid convergence, fillets with radius 1.27 mm (0.0500 in) are used at all corners involved
153 in contact definitions.

154 Prefabrication is first modeled, using the validated approach developed in Gerbo et al. (2016),
155 to provide an initial strain state in the plates which is imported into the field installation model.
156 This ensures that the steel hardness in the prebent region of the plates is properly simulated.

157 Bolt tightening is achieved through a prescribed relative displacement between the inside of
158 the nut and the tip of the bolt (Figure 4A and 4B), modeling the displacement achieved in the
159 experimental procedure. After completion of tightening, the bolt is released from its interactions to
160 simulate the disassembly process. For comparison with the measured data, the predicted FE plate
161 strains are those at full tightening. Predicted bolts strains are residual strains after disassembly.

162 The thread interaction between the nut and bolt is not modeled, but a reduced cross-section
163 based on measurements of the bolt (28.5% reduction) is used in the threaded region for all reported
164 bolt data. For the models predicting the plate strains, a constant cross-section cylindrical bolt was
165 used due to numerical issues in predicting plate strains near the plate-bolt contact.

166 In the FE models of the experimentally tested scenarios, extra washers and spacers (which
167 facilitated testing) were used to replicate the physical assembly. This hardware was simplified in
168 the parametric models to include only a single washer at the bolt head to plate contact, and a single
169 washer at the nut to plate contact, resulting in shorter bolts required to reach through the connection
170 hardware. The bolt lengths in the parametric models vary based on the grip length [i.e., twice the
171 plate thickness (t_s) plus the member thickness (t_m)].

172 **BEHAVIOR OF BOLTS AND PLATES DURING FIELD INSTALLATION**

173 During field installation, the bolts are placed in axial tension by tightening. This tension is
174 resisted by bending in the plates until contact with the member. After contact, additional bolt
175 tension applies a clamping force between the plies of the member and plates, providing resistance
176 to slip under loading. As the plies are non-flush, combined tension and bending occurs during
177 bolt tightening due to the eccentric contact at the bolt head and nut, causing bending in the bolts.
178 Additional bending results from contact with the plate holes. The resulting strain pattern is a
179 combination of tension and bending [e.g., Figure 3, where bending in Scenario 1 is indicated with
180 regions of concentrated tension (blue) and compression (red) along the bolt shank]. Figure 5 shows
181 the amount and location of bolt bending in Scenario 1 by plotting the curvature (ϕ) as a function of
182 longitudinal coordinate of the bolt. Curvature is calculated by fitting planes to the longitudinal bolt
183 surface strains (ϵ_y), which are divided into regions perpendicular to the bolt axis creating many

184 section cuts. The slope of the fitted planes, relative to the longitudinal (z) axis, is the curvature. A
185 moving average is then used to smooth out noise from this plane fitting process. The location of the
186 curvature for Scenario 1, i.e., along the bolt shank as opposed to the reduced regions, indicates that
187 bolt bending is primarily due to contact with the plates. In contrast, a flush slip-critical connection
188 (Scenario 14) featured measured and predicted strains that were only axial (data not shown for
189 conciseness).

190 **Effect of Bolt Tightening Procedure**

191 Due to the relatively large number of turns required to close the adjustable connection (varying
192 from 3 to 12 turns), compared to a conventional connection with initially flush plies, it is desirable
193 to minimize the time required to install the connection. One means of reducing construction time
194 is to increase the number of bolt turns completed in each increment. When using single turn
195 increments in a criss-cross pattern (Scenario 1), the measured longitudinal surface bolt strains are
196 predominantly symmetric among the four bolts (Figure 3). Small differences are observed in the
197 lower bending region [i.e., $y = -40.0$ mm (1.57 in.)], where bolts 1 and 2 (Figure 1D) experience
198 tensile strains up to 0.0447 mm/mm, bolt 3 experiences 0.0483 mm/mm and bolt 4 experiences just
199 0.0411 mm/mm]. This localized asymmetry is likely caused by the tightening procedure which
200 proceeded from bolt 1 to bolt 4 for Scenario 1. Figure 5 shows similar locations and magnitudes
201 of curvature for Scenario 1 among the four bolts (with peak curvature magnitudes ranging from
202 0.113 deg/mm to 0.186 deg/mm, a difference of less than 40 percent).

203 By increasing the number of turns per tightening increment to 3 (Scenario 2), the measured
204 longitudinal surface strains in bolts 3 and 4 are higher than bolts 1 and 2 (with bolts 3 and 4
205 reaching strain magnitudes of 0.0710 mm/mm and bolts 1 and 2 reaching 0.0657 mm/mm). The
206 measured curvature in bolts 3 and 4 (with peak magnitudes of 0.290 deg/mm) is also much higher
207 than bolts 1 and 2 (with peak magnitudes of 0.141 deg/mm), as well as higher than all bolts of
208 Scenario 1 (Figure 5). The lower strains and curvature in the first two bolts are due to rigid body
209 movement of the plates during the first turns which reduces the bolt deformation. The increased
210 strains and curvature in bolts 3 and 4 are due to the additional restraint imposed by the tightening

211 of the first two bolts, therefore increasing the required bolt deformation at contact with the plates
212 for the last two bolts. Increasing the increment further, such that each bolt is tightened to contact
213 before moving onto the next bolt (Scenario 3) resulted in fracturing bolt 3. This combined tension
214 and torsion failure caused a fracture in the threaded region of the 165 mm (6.5 in.) long A325
215 bolts that closed the 50.5 mm (1.99 in.) total thickness of plies. Therefore, to achieve relatively
216 uniform strains and curvature among the bolts, the recommended procedure is 1 turn of each bolt
217 per increment. This is consistent with the recommendations in Gerbo et al. (2018) to maintain
218 symmetric strains in the plates.

219 The tightening pattern (criss-cross, clockwise, or counter-clockwise), while maintaining 1 turn
220 per increment, was investigated by comparing bolt strains in Scenarios 1, 4, and 5. All three
221 scenarios resulted in similar distributions and magnitudes of strains in the bolts (full-field data for
222 Scenarios 4 and 5 not shown for conciseness). The curvature in all bolts for both Scenario 4 and 5
223 are similar to one another and similar to Scenario 1 (Figure 5). It was found in Gerbo et al. (2018)
224 that circular tightening procedures (i.e., Scenarios 4 and 5) lead to diagonal strain banding in the
225 plates. Therefore it is recommended to use a criss-cross tightening pattern for field installation. All
226 scenarios discussed throughout the rest of the paper use the recommended tightening procedure of
227 1 turn per increment in a criss-cross pattern.

228 The FE models feature only one bolt (due to symmetry) and assume a uniform, simultaneous
229 bolt tightening procedure. The FE predictions accurately capture the peak measured bolt strains
230 (with peak predicted longitudinal strains of 0.0510 mm/mm and peak measured longitudinal strains
231 ranging from approximately 0.0310 mm/mm to 0.0514 mm/mm) and curvatures (with peak pre-
232 dicted curvature of 0.202 deg/mm and peak measured curvatures ranging from 0.113 deg/mm to
233 0.186 deg/mm) with the recommended tightening procedure of 1 turn per increment in a criss-
234 cross pattern (Scenario 1). The differences between the FE predictions and the measured results in
235 Scenario 2 (with measured peak curvatures ranging from 0.103 deg/mm to 0.305 deg/mm) can be
236 attributed to the asymmetric behavior that occurs with this tightening increment which could not
237 be captured by a symmetric FE model.

238 **Effect of Varying Amount and Direction of Plate Bend**

239 Varying the amount of plate bending (i.e., the magnitude of δ) and the direction of plate bending
240 (i.e., the sign of δ , where positive indicates further bending and negative indicates bending back
241 toward flat) affects bolt behavior during field installation. During plate bending, bolts are subjected
242 to bending from eccentric bolt head and nut contact and from plate contact on the shank of the bolt.
243 An indicator of bolt bending is the amount of bolt deformation (e_b , Figure 2C, Table 1) which can
244 be approximated as:

$$e_b = e_h - (d_{ph} - d_b) \quad (1)$$

245 where e_h is the eccentricity between the plate holes, calculated as:

$$e_h = e_o + \frac{e_d}{\cos \alpha} \quad (2)$$

246 where e_o is the eccentricity due to the vertical offset of the plates relative to the member angle and
247 e_d is the effect of the deformed shape on horizontal component of the plate lengths (Figure 2C-E).
248 Assuming the deformed shapes of the top and bottom plates have identical profiles in elevation and
249 are axially rigid, e_o is calculated as follows:

$$e_o = |(t_m + t_s) \tan \alpha| \quad (3)$$

250 To account for the difference in deformed profiles of the top and bottom plates, an approximation
251 can be made that the plates are composed of two rigid bodies connected by a plastic hinge. If δ is
252 positive, the plastic hinge in the top plate will occur at the member contact location and the plastic
253 hinge in the bottom plate will occur at the net section. If δ is negative, the opposite is true. The
254 change in the horizontal components of the plate lengths due to this simplified deformed shape (e_d)
255 is calculated as follows:

$$e_d = \begin{cases} l_4(\cos \gamma - \cos \alpha) & \text{if } \delta \geq 0 \\ g(\cos \gamma - \cos \alpha) & \text{if } \delta \leq 0 \end{cases} \quad (4)$$

256 where l_4 is the distance from the edge of the member to the center of the member hole and g is the
 257 gap between the members at the top flange (Figure 2). Note that these approximations assume the
 258 holes are smaller in the plates (i.e., oversized holes) than in the member (i.e., long slots).

259 High values of bolt deformation, e_b , correspond to higher longitudinal strains and curvature
 260 in the bolts, as shown for example in Scenario 1 ($\delta = 7.5^\circ$, Figures 3 and 6). By decreasing the
 261 amount of bending and therefore reducing e_b , the magnitude of curvature in Scenario 6 ($\delta = 2.5^\circ$)
 262 is reduced (Figure 6). The distribution of curvature along the bolt length remains the same, with
 263 concentrations along the bolt shank at contact locations with the plates demonstrating plate contact
 264 as the primary contributor to bending.

265 When the direction of plate bending is reversed in Scenario 8 ($\delta = -7.5^\circ$), the bolt deformation,
 266 e_b is reduced as the plates are bent back toward flat and are no longer in contact with the bolt. The
 267 measured full-field strains show almost no strain in the bolt shank and reduced data loss (compared
 268 to Scenario 1) from gouging which indicates limited plate contact. The FE predictions indicate that
 269 strains are concentrated in the reduced cross-section representing the threaded region. Increased
 270 curvature is also predicted in the reduced cross-section (Figure 6). The location of this curvature
 271 in the reduced cross-section indicates that bending is primarily due to eccentric contact of the bolt
 272 head and nut. A reduced magnitude of plate bending in Scenario 7 ($\delta = -2.5^\circ$) results in similar
 273 strain and curvature distributions (Figure 6), with lower magnitudes.

274 Figure 7 shows the relationships between e_b and curvature for the experimentally tested sce-
 275 narios. Here the curvature is calculated separately for the bolt shank compared to the reduced
 276 cross-section. Note that the curvature values are from the FE models as these are better able to
 277 capture curvature in the threaded region of the bolts (modeled as a reduced cross-section). High
 278 values of e_b [i.e., $e_b > 3.18$ mm (0.125 in.)] indicate bending predominantly in the bolt shank due
 279 to plate contact. The reduced cross-section is sufficiently far from the shear plane (as spacers to

280 facilitate the experimental program move the threaded region beyond the shear plane) to not be
281 affected by this bending. However, there is some bending indicated by the small peak curvature
282 in the reduced cross-section. Conversely, small value and negative values of e_b [i.e., $e_b < 3.18$
283 mm (0.125 in.)] feature peak curvature in the reduced cross-section as bending is dominated by
284 eccentric bolt head and nut contact.

285 **Effect of Varying Plate Angle**

286 These trends relating the bolt deformation (e_b) to the bending in the bolts are also observed for
287 varying plate angles ($\gamma = \beta$), considering bending of $\delta = \pm 2.5^\circ$.

288 In scenarios with low initial plate angles (i.e., $\gamma = \beta \leq 10^\circ$, Scenarios 9, 10, and 11), the
289 induced strains are concentrated in the reduced cross-section (data not shown for conciseness).
290 Consistent with prior findings for scenarios with low e_b , the curvature is predominantly in the
291 reduced cross-section region, indicating bending from eccentric bolt head and nut contact (Figure
292 7 and 8).

293 Scenarios with high initial plate angles (i.e., $\gamma = \beta \geq 10^\circ$, Scenarios 12 and 13) show similar
294 trends with e_b . Scenario 13, with a high value of e_b , exhibits high curvature in the bolt shank
295 region, indicating bending due to plate contact (Figure 7 and 8). Scenario 12, with a much lower
296 value of e_b , shows almost no bending.

297 The numerical predictions for Scenario 13 indicate a higher magnitude of curvature at the top
298 bending location [0.215 deg/mm (5.46 deg/in.) peak curvature at $y = 8.01$ mm (0.315 in.)] than
299 the bottom bending location [0.0100 deg/mm (0.254 deg/in.) at $y = -39.6$ mm (1.56 in.)]. This
300 is in contrast to the measured data which indicates more symmetric curvature at both of the plate
301 contact locations. The FE models for this type of scenario (i.e., positive δ) show that the bending
302 in the bolts occurs first at the top plate contact location followed by bending at the bottom plate
303 contact location at the last part of tightening. Bending at the top plate location occurs first because
304 the bolt force is higher nearer the tightening location as compared to the bottom plate location
305 where frictional losses reduce the force in the bolt. The FE model for Scenario 13 shows that
306 while the plates and members are in contact (per the experimental protocol) and an additional turn-

307 of-nut was also performed, the spacer by the head of the bolt does not come into firm contact with
308 the washer. The DIC photographs of this scenario confirm this condition, but to a lesser degree.
309 Additional FE modeling indicated that if the bolt were tightened an additional turn, bending would
310 have occurred also at the bottom plate contact location, and the spacers would come into firm
311 contact with the washers. This demonstrates that more strict tightening criteria, which requires
312 firm contact between the bolt head, washer, and plates, are needed. This will be investigated in
313 future research focusing on the connection strength. Scenario 13 was particularly susceptible to
314 this effect because it features the highest plate angle ($\gamma = \beta = 15^\circ$) and bends to the highest member
315 angle ($\alpha = 17.5^\circ$).

316 **Summary**

317 The field bending process induces residual strains in the bolts in both axial and bending domi-
318 nant patterns. The magnitude of bending is related to the bolt deformation (e_b) which also indicates
319 if the bending is from plate contact in the bolt shank region [$e_b > 3.18$ mm (0.125 in.)] or from
320 eccentric bolt head and nut contact resulting in bending in the threaded region [$e_b < 3.18$ mm
321 (0.125 in.)]

322 Overall, the FE predictions agree closely with the measured results, both in the distribution and
323 magnitude of longitudinal bolt strains. Through these comparisons, the FE modeling approach can
324 be considered validated with respect to the bolt strains induced during field installation.

325 **NUMERICAL PREDICTIONS OF PLATE STRAINS**

326 To validate the numerical modeling approach with respect to the plate behavior, FE predictions
327 for circumferential plate surface strains (ϵ_x , i.e., strain in the x direction in Figure 9) were compared
328 with measured results. The measured strain induced during field installation [reported in Gerbo
329 et al. (2018)], as well as the measured cumulative strains from prefabrication [reported in Gerbo
330 et al. (2016)] and field installation (cumulative fabrication process, hereafter) are compared to the
331 FE predictions.

332 **Benchmark Comparison**

333 The measured and predicted full-field circumferential strains of a benchmark case [Scenario
334 6, selected because it is between the minimum and maximum considered member angles (α), and
335 follows the $|\delta| \leq 2.5^\circ$ recommendation of Gerbo et al. (2018)] show close agreement in magnitude
336 and distribution (Figure 10), for both the field bending and cumulative fabrication process. FE
337 predictions of the field bending process indicate peak circumferential surface strains of 0.00467
338 mm/mm in the top plates and -0.00291 mm/mm in the bottom plates. The predicted field bending
339 strains in the bottom plate are spread out smoothly over the center region [approximately 50-100
340 mm (2-4 in.) width] of the plate, whereas the predicted field bending strains in the top plate are
341 concentrated more locally [approximately 20-30 mm (0.8-1.2 in.) width], directly over the contact
342 locations with the member. Circumferential surface strain data is also plotted along longitudinal
343 Lines A-D (Figure 9) on the plate surfaces (Figure 11). Generally, the measured and predicted
344 data agree closely. However, the measured peak field bending strains in the top plate are higher
345 in magnitude (reaching 0.0102 mm/mm) than the predicted results (0.00467 mm/mm) along Lines
346 B and C at $x = 90$ mm (3.54 in.). This can be attributed to a combination of asymmetry in the
347 reaction frame and the bolt tightening process (Gerbo et al., 2018). The FE model is unable to cap-
348 ture these effects because it assumes symmetry across two planes and therefore assumes uniform
349 simultaneous bolt tightening and a perfect reaction frame.

350 The cumulative strain patterns are dominated by the prefabrication process (Figure 10 and 11).
351 The peak predicted and measured cumulative strains in Scenario 6 occurs in the prebent region of
352 the top plate. The small predicted strain concentrations along Lines B and C at $x = 90$ mm (3.54
353 in.) due to contact with the member during field bending are an order of magnitude lower than
354 strains induced during prefabrication and are insignificant in comparison to the cumulative strains
355 (approximate peak strains of 0.06 mm/mm). The cumulative strains in the bottom plates are even
356 less affected by the field bending process, representing almost solely the prefabrication process.

357 Overall, the measured results agree well with the FE predictions.

358 **Varying Amount and Direction of Plate Bend**

359 Figure 11 demonstrates that the FE modeling approach is valid for varying amounts and direc-
360 tion of bending. The field bending strains are affected by the prefabrication process as the cold
361 bending via press brake induces an initial strain state in the center region, locally hardening the
362 steel. This alters the distribution of field bending strains when field bending strains coincide with
363 prefabrication strains in environments of positive δ (Gerbo et al., 2018). For example, the peak
364 field bending strains are pushed to the edge of the prebent region in the bottom plates of Scenario 1
365 (see Lines A and D in Figure 11). This is also present in Scenario 6, but is less clearly observed as
366 field bending strains are lower due to the smaller δ . This demonstrates the importance of including
367 the initial strain state in the FE models.

368 There are a few locations where the measured results and FE predictions for field bending
369 strains differ. The measured strains are approximately double the predicted FE strains in Scenario
370 8 along Line A and D in the prebent region of the bottom plates. This is because Scenario 8 induces
371 significant bending in the direction opposite that of fabrication. The Bauschinger effect lowers the
372 yield stress due to this reversal of plastic strain in the prebent portion of the plates. The FE material
373 model used an isotropic hardening model that does not incorporate the Bauschinger effect, and thus
374 predicts lower strain magnitudes from field bending than the measured DIC results for Scenario 8
375 in the prebent region. This could be improved by the use of a kinematic hardening model, although
376 the effect is minor in comparison to the overall magnitude of the cumulative strains. This trend is
377 also observed in Scenario 7, but to a lesser extent due to the lower magnitude of δ .

378 Scenario 8 exhibits a measured peak field bending strain of 0.0171 mm/mm along Line A at
379 the location of contact with the member on the left side, which is not seen on the right side of
380 the measured results or in the FE predictions (Figure 11). This can be attributed to a combination
381 of imperfections in the reaction frame and asymmetry in bolt tightening (Gerbo et al., 2018). As
382 discussed in reference to Scenario 6, this shows that some asymmetry is to be expected during field
383 bending which cannot be captured by a symmetric FE model.

384 For Scenario 1, along lines B and C, the numerical models tend to overpredict the measured

385 peak field bending strain at the member contact locations by approximately 10-15%. This is par-
386 tially due to the strain measurement length used in the DIC calculations [the gauge length is 2.91
387 mm (0.114 in.) which is nearly double the mesh size in the FE models]. The resulting data av-
388 eraging in DIC reduces the value of localized peaks. Another potential factor is the radius of the
389 fillet [1.27 mm (0.0500 in.)] used for all of the FE models. This value was selected based on
390 approximate fillet radius measurements of the fabricated frame which varies due to the irregular
391 nature of manually softening edges with an angle grinder. Further numerical modeling found that
392 a larger fillet radius in the member at the point of contact with the top plate will result in a reduced
393 peak strain [e.g., for a 3.81 mm (0.150 in.) radius, the predicted peak strain reduced by 24% on the
394 compressive face and by 3% on the tensile face]. Scenario 1 is particularly susceptible to the data
395 averaging and fillet radius issues because it has a high positive δ localizing strain at the member
396 contact location.

397 Overall, the prefabrication process dominates the cumulative strains in all scenarios (Figure
398 11). Any small differences between measured and predicted field bending strains discussed above
399 are negligible compared to the cumulative strains. Both the measured and predicted cumulative
400 strains are all very similar in the prebent region of the top plate. The predicted cumulative strains in
401 the prebent regions of the bottom plates differ more from the measured results (i.e., 20% difference
402 in the peak cumulative strain in Scenario 8) than the top plates (i.e., 5% difference in the peak
403 cumulative strains in Scenario 8) due to the Bauschinger effect.

404 **Summary**

405 The developed FE modeling approach is able to predict circumferential surface strain distribu-
406 tions and magnitudes in the plates from field bending and the cumulative fabrication process for a
407 wide variety of scenarios, including varying amount and direction of plate bend as well as varying
408 plate angle (data for Scenarios 9-13 not shown for conciseness). Cumulative strains are dominated
409 by prefabrication and the numerical modeling approach is capable of accurately capturing these
410 cumulative strains. The simplifying assumptions of symmetric bolt tightening and idealized ge-
411 ometry of the reaction frame have negligible impact on the ability of the FE models to accurately

412 capture plate behavior during field bending and the cumulative fabrication process. The isotropic
413 material model, which does not account for the Bauschinger effect, resulted in small differences
414 between the measured and predicted field bending strains. However, these are insignificant com-
415 pared to the magnitude of the cumulative strains.

416 **PARAMETRIC STUDY**

417 With the numerical FE modeling approach validated, a parametric study was performed to
418 investigate the effect of (1) bolt diameter (d_b), (2) plate thickness (t_s), and (3) member thickness
419 (t_m) on residual bolt strains from field installation and on plate circumferential surface strains from
420 field bending and the cumulative fabrication process. The plate bend radii were varied to maintain
421 a constant ratio of radius to plate thickness ($r_b = r_t = 8t_s$). By maintaining the radius-to-plate-
422 thickness ratio, the magnitude of the peak prefabrication strains in the plates is approximately the
423 same, though the width of the prebent section varies. A total of 11 scenarios were investigated
424 in comparison to a benchmark (Scenario A) with the same bolt diameter (d_b), plate thickness (t_s),
425 and member thickness (t_m) as studied in the experimental program. The plate angles ($\gamma = \beta =$
426 10°), member angles ($\alpha = 12.5^\circ$), and relative ply angles ($\delta = 2.5^\circ$) were constant and the same as
427 Scenario 6.

428 **Effect of Bolt Diameter**

429 Increasing the bolt diameter reduces bolt strains induced by field bending in most Scenarios,
430 as expected (Figure 12). In comparison to the experimental program (e.g., Figure 3), the peak
431 strains are concentrated in the reduced cross-section as opposed to the bolt shank for all parametric
432 results. This is because the experimentally tested bolts had longer shanks (to facilitate testing pro-
433 tocol) which pushed the threaded region away from the shear plane. The parametric results have
434 more realistic bolt shank lengths (due to elimination of the spacers used to facilitate experimen-
435 tal testing), such that the reduced cross-section, while still not in the shear plane, is much closer.
436 This concentrates bending strains, even from plate contact, in the reduced cross-section. Figure 13
437 shows the peak magnitude of curvature for the parametric scenarios, indicating curvature predom-
438 inantly in the reduced cross-section.

439 Scenario G (most conservative) uses 25.4 mm (1.00 in.) diameter bolts to tighten 12.7 mm
440 (0.500 in.) thick plates, resulting in bolt strains below 0.0277 mm/mm. This is predominantly
441 axial strain, as demonstrated by the low peak curvature [0.0226 deg/mm (0.574 deg/in.)]. Scenario
442 C (least conservative) uses 19.2 mm (0.750 in.) diameter bolts to tighten 19.2 mm (0.750 in.) thick
443 plates, resulting in noticeable bending with peak tensile strains of 0.109 mm/mm, peak compressive
444 strains of 0.130 mm/mm, and peak curvature of 0.461 deg/mm (11.7 deg/in.) (Figure 12). In
445 general, the bending and therefore curvature increases with increasing bolt deformation (e_b) as
446 found in the experimental results (Figure 13). However, Scenario F, which has the same e_b value
447 as Scenario C, has lower peak curvature [0.354 deg/mm (8.99 deg/in.)] yet higher strains (0.133
448 mm/mm peak tensile strains and 0.195 mm/mm peak compressive strains). This is because the
449 the larger bolt diameter than Scenario C (17% difference) requires higher strain (22% higher peak
450 tensile strain and 50% higher peak compressive strain than Scenario C) to accommodate the same
451 high bolt deformation (e_b).

452 Figure 14 shows that the bolt diameter is weakly inversely proportional to the induced field
453 bending strains in the plates (focusing on strains away from the bolt hole locations), with larger
454 bolts leading to slightly lower plate strains than smaller bolts. This is due to the larger area over
455 which the clamping force is induced, leading to more evenly distributed strains during the field
456 bending process. The cumulative strains for a given plate thickness are not significantly impacted
457 by bolt diameter as they are dominated by the prefabrication strains.

458 **Effect of Plate Thickness**

459 For a given bolt diameter, an increase in plate thickness results in higher bolt strains (Figure
460 12) and higher bolt curvature (Figure 13). For a bolt diameter of 19.1 mm (0.750 in.) (Scenarios
461 A, B and C), the peak induced tensile strain varies from 0.0510 mm/mm to 0.109 mm/mm for plate
462 thicknesses of 12.7 mm (0.500 in.) to 19.1 mm (0.750 in.), respectively, and the peak curvature
463 increases from 0.241 deg/mm (6.12 deg/in.) to 0.461 deg/mm (11.7 deg/in.). This is partly due
464 to the additional bolt force required to close connections with thicker plates, resulting in a higher
465 moment from eccentric bolt head and nut contact. The bolt bending is also increased by thicker

466 plates because the eccentricity between the plate holes (e_h) increases, which results in larger re-
467 quired bolt deformation (e_b). The bolt deformation is found to be positively correlated with the
468 peak bolt strain (Figure 12) and peak curvature (Figure 13). It is therefore recommended that the
469 bolt deformation (e_b) be below 3.18 mm (0.125 in.) to minimize bolt bending.

470 The relationship between plate thickness and peak bolt strain is most significant in the smallest
471 bolts [$d_b = 19.1$ mm (0.75 in.), Scenarios A, B and C], and least significant in the largest bolts [$d_b =$
472 25.4 mm (1.00 in.), Scenarios G, H and I] (Figure 12). This is likely due to the larger bolts having
473 a higher yield force, and therefore lower degrees of plastic behavior compared to the smaller bolts.
474 Recall that only plastic residual strains are reported. When considering the difference between
475 the thinnest and thickest plates, the peak tensile strain increases from 0.0277 mm/mm to 0.0316
476 mm/mm for the largest diameter bolts (i.e., Scenarios G - I), and from 0.0510 mm/mm to 0.109
477 mm/mm for the smallest diameter bolts (Scenarios A - C) (Figure 12). In order to keep the bolt
478 from experiencing significant increases in strain, it is recommended to use bolts with a diameter at
479 least 20% greater than the plate thickness (e.g., Scenario B).

480 The predicted peak field bending strains in the plates at the member contact locations are not
481 significantly affected by the plate thickness (Figure 14). The cumulative plate strains are dominated
482 by the prefabrication process, discussed in Gerbo et al. (2016), with field bending strains being an
483 order of magnitude lower.

484 **Effect of Member Thickness**

485 Member thicknesses were varied to explore the plate and bolt behavior with more flexible
486 members, corresponding to W10x88, W10x68 and W10x49 sections (Table 2). Connections with
487 thicker members (i.e., Scenario A) are found to induce higher bolt bending strains (Figure 15) and
488 curvature (Figure 13) than thinner members (i.e., Scenario K). This is because thicker members
489 result in higher required bolt deformation (e_b).

490 A flexible (i.e., thin) member flange deforms more during field bending and therefore can
491 reduce the peak field bending strains in the plates at the member contact locations along lines B
492 and C. It is found that a thinner member flange results in lower induced plate strains during field

493 bending as expected. This difference is most significant between the thickest member flanges [t_m
494 = 25.1 mm (0.990 in.), Scenario A] and the thinnest member flanges [$t_m = 14.2$ mm (0.560 in.),
495 Scenario K], with a 26.2% reduction in peak field bending strain in the top plates, and a 12.2%
496 reduction in the bottom plates. The cumulative strains are nearly indistinguishable between these
497 three scenarios, as the minor differences in the field bending strains are overshadowed by the
498 prefabrication strains.

499 **Local Plate Strains**

500 Local strain concentrations occur in the plates near the bolt holes [i.e., $x = \pm 150$ mm (5.91 in.)
501 on lines B and C in Figure 14] and are positively correlated with the bolt deformation (e_b). These
502 strain concentrations can somewhat be seen in the measured results near this region in Figure 11.
503 However, the measured strains are lower in magnitude than the FE predictions partially due to the
504 DIC view being blocked by the washers and bolt assembly, as well as the edge effect observed
505 in DIC measurements as discussed in Gerbo et al. (2016). The FE models are therefore useful
506 tools to be able to determine the peak strains near the bolt hole, not only on the plate surface but
507 also through the thickness of the plate. Increasing e_b results in increased local strains near the
508 plate holes due to the additional contact pressure between the bolt and the plate hole (Figure 16).
509 To keep local strains in the plates below the recommended 0.100 mm/mm [strains beyond 0.100
510 mm/mm have been found to result in reductions to ductility and fracture toughness (Keating and
511 Christian, 2012)], e_b should be kept below 3.18 mm (0.125 in.).

512 **CONCLUSIONS**

513 This paper presented an experimental investigation of bolt behavior in adjustable bolted steel
514 plate connections during field installation, a validated numerical modeling approach, and a numer-
515 ical parametric investigation of the impact of (1) bolt diameter, (2) plate thickness, and (3) member
516 flange thickness on the strains induced in both the plates and bolts during field installation. Based
517 on these experimental and numerical studies, the following conclusions are made. Note that these
518 conclusions may only be relevant to the specific scenarios studied in this research.

- 519
- 520 • A bolt tightening procedure using 1 turn increments and a criss-cross pattern is recom-
521 mended to ensure evenly distributed strains in the four bolts of the connection, consistent
522 with the recommendations in Gerbo et al. (2018) for evenly distributed plate strains. Tight-
523 ening procedures with 3 or more turns per increment were found to result in gouging to
524 the surface of the bolt, and significant asymmetries in strains among the four bolts of the
525 connection. By using 1 turn increments, the bolts are evenly tightened, resulting in more
uniform behavior across the connection.
 - 526 • Prefabrication strains (approximately 0.06 mm/mm) dominate behavior of the plates com-
527 pared to field bending strains (approximately 0.006 mm/mm) by an order of magnitude.
528 Recommendations regarding the strains induced during prefabrication are discussed in
529 Gerbo et al. (2016). The parameters chosen for prefabrication (i.e., bend radius and plate
530 thickness) play a more significant role in determining cumulative strains than the parame-
531 ters chosen during field bending.
 - 532 • The bolt deformation (e_b) should not exceed 3.18 mm (0.125 in.) to reduce bolt bending
533 strains and to reduce local strain concentrations in the plates near the bolt holes. Consider-
534 ing the formulation for e_b and the shallow member angles (α) investigated in this research,
535 the most effective means of reducing e_b is to reduce the bolt diameter (d_b) or increase the
536 plate hole diameter (d_{ph}), with reduced benefit from decreasing the member thickness (t_m)
537 or the plate thickness (t_s). Reducing the bolt diameter (d_b) could have a negative impact
538 on connection performance, which will be an area of future research. Increasing the plate
539 hole diameter (d_{ph}), beyond the currently investigated oversized holes, may also negatively
540 impact connection performance and potentially also durability.
 - 541 • To ensure adequate bolt strength to close a given connection, it is recommended to use bolt
542 diameters (d_b) at least 20% larger than the plate thickness (t_s). However, increased bolt
543 diameter can have a negative impact on connections with high e_b values, as it can increase
544 the bolt bending strains. Bolt diameter is weakly inversely proportional to the magnitude
545 of the induced field bending strains in the plates.

- 546 • Thinner member flanges can lower the strains induced in the plates during field bending by
547 up to approximately 26%. More flexible members [i.e., $t_m \leq 19.6$ mm (0.770 in.)] conform
548 more to the plates' initial shape, while inducing negligible strains in the member. Member
549 thickness (t_m) does not play a direct role in the induced strain in the bolts. However, it is
550 used in the calculation of e_b , and therefore can indirectly affect bolt bending.

551 The adjustable bolted steel plate connection shows promise to provide adjustability in steel
552 plate connections, and to accommodate significant construction and manufacturing tolerances. Fu-
553 ture work includes evaluation of connection performance under service and ultimate limit states.

554 Importantly, the research findings provide useful limits on bolt tightening procedures, bolt
555 deformation (e_b), and relative sizes of bolts and plates for any misaligned (non-flush) bolted splice
556 connections. This enables force fitting to be performed in a controlled manner in which the strains
557 induced in the bolts and plates during bolt tightening are well understood. The future research
558 in understanding the connection performance under service and ultimate limit states will provide
559 further guidance on these procedures.

560 **ACKNOWLEDGMENTS**

561 This material is based upon work supported by the National Science Foundation under Grant
562 No. CMMI-1351272. The support of Program Managers Drs. Kishor Mehta and Y. Grace Hsuan
563 is gratefully acknowledged.

564 **REFERENCES**

- 565 AASHTO (2014). *AASHTO LRFD Bridge Design Specifications, Customary U.S. Units*. American
566 Association of State Highway and Transportation Officials (AASHTO), 7th Edition, with 2015
567 and 2016 Interim Revisions, Washington, D.C.
- 568 ABAQUS (2014). “ABAQUS/Standard Analysis User’s Manual Version 6.14. Dassault Systemes,
569 Waltham, MA.
- 570 ASTM (2014a). “ASTM A325-14: Standard specification for structural bolts, steel, heat treated,
571 120/105 ksi minimum tensile strength.” ASTM International. West Conshohocken, PA.
- 572 ASTM (2014b). “ASTM A36/A36M-14: Standard specification for carbon structural steel.”
573 ASTM International. West Conshohocken, PA.
- 574 ASTM (2015). “ASTM A992-15: Standard specification for structural steel shapes.” ASTM Inter-
575 national.
- 576 ASTM (2018). “ASTM F436/F436M-18a: Standard specification for hardened steel washers inch
577 and metric dimensions.” ASTM International. West Conshohocken, PA.
- 578 Chesson, E. and Munse, W. H. (1965). “Studies of the behavior of high strength bolts and bolted
579 joints.” *Engineering Experiment Station*, University of Illinois, 469.
- 580 Douty, R. T. and McGuire, W. (1965). “High strength bolted moment connections.” *Journal of the*
581 *Structural Division*, American Society of Civil Engineers, 91(ST2), 101–128.
- 582 Ferro (2016). “CerMark laser marking materials. [http : //www.ferro.com/Our +](http://www.ferro.com/Our+Products/ColorsGlass/FunctionalIndustrial/CerMark/)
583 [Products/ColorsGlass/FunctionalIndustrial/CerMark/](http://www.ferro.com/Our+Products/ColorsGlass/FunctionalIndustrial/CerMark/) (January 26, 2016).
- 584 Gerbo, E. J., Thrall, A. P., Smith, B. J., and Zoli, T. P. (2016). “Full-field measurement of residual
585 strains in cold bent steel plates.” *Journal of Constructional Steel Research*, 127, 187–203.

586 Gerbo, E. J., Wang, Y., Tumbeva, M. D., Thrall, A. P., Smith, B. J., and Zoli, T. P. (2018). “Behavior
587 of an adjustable bolted steel plate connection during field installation.” *Journal of Structural*
588 *Engineering*, 144(3) , 04017223.

589 Gerbo, E. J., Wang, Y., Tumbeva, M. D., Thrall, A. P., Smith, B. J., and Zoli, T. P. (2019). “Closure
590 to ‘Behavior of an Adjustable Bolted Steel Plate Connection during Field Installation’ by Evan
591 J. Gerbo, Yao Wang, Mirela D. Tumbeva, Ashley P. Thrall, Brian J. Smith, and Theodore P.
592 Zoli.” *Journal of Structural Engineering*, 145(3) , 07018015.

593 Keating, P. B. and Christian, L. C. (2012). “Effects of bending and heat on the ductility and fracture
594 toughness of flange plate. Technical Report No. FHWA/TX-10/0-4624-2.

595 Kulak, G. L., Fisher, J. W., and Struik, J. H. A. (2001). *Guide to Design Criteria for Bolted and*
596 *Riveted Joints*. American Institute of Steel Construction, 2nd Edition, Chicago, I.L.

597 Munse, W. H., Peterson, K. S., and Shesson, E. (1959). “Strength of rivets and bolts in tension.”
598 *Journal of the Structural Division*, American Society of Civil Engineers, 85(ST3), 7–28.

599 Rajasekharan, N. S., Birkemoe, P. C., and Munse, W. H. (1974). “High strength bolts subject to
600 tension and prying.” *Journal of the Structural Division*, American Society of Civil Engineers,
601 100, 351–372.

602 Research Council on Structural Connections (2014). “Specifications for Structural Joints Using
603 High-Strength Bolts.

604 **List of Tables**

605 1 Experimentally tested connection parameters. * Abbreviations for bolt tightening
606 procedure, with indications for bolt number: (x) = criss-cross (1-2-3-4), (cw) =
607 clockwise (1-4-2-3), (ccw) = counter-clockwise (4-1-3-2) (Figure 1). 26

608 2 Parametric study connection parameters. Bolded scenario indicates benchmark
609 case. Initial plate angles ($\gamma = \beta = 10^\circ$), member angles ($\alpha = 12.5^\circ$), and relative
610 ply angles ($\delta = 2.5^\circ$) are constant. 27

TABLE 1. Experimentally tested connection parameters. * Abbreviations for bolt tightening procedure, with indications for bolt number: (x) = criss-cross (1-2-3-4), (cw) = clockwise (1-4-2-3), (ccw) = counter-clockwise (4-1-3-2) (Figure 1).

Scenario	$\gamma = \beta$ (deg.)	α (deg.)	δ (deg.)	$l_1=l_2$ (mm)	Tightening Procedure Increment (Pattern*)	e_b (mm)
1	10	17.5	7.5	483	1 turn/bolt (x)	9.65
2	10	17.5	7.5	483	3 turns/bolt (x)	9.65
3	10	17.5	7.5	483	Fully tighten bolt (x)	9.65
4	10	17.5	7.5	483	1 turn/bolt (cw)	9.65
5	10	17.5	7.5	483	1 turn/bolt (ccw)	9.65
6	10	12.5	2.5	483	1 turn/bolt (x)	4.29
7	10	7.5	-2.5	483	1 turn/bolt (x)	-0.377
8	10	2.5	-7.5	483	1 turn/bolt (x)	-4.25
9	0	2.5	2.5	381	1 turn/bolt (x)	-3.04
10	5	2.5	-2.5	432	1 turn/bolt (x)	-3.28
11	5	7.5	2.5	432	1 turn/bolt (x)	0.585
12	15	12.5	-2.5	533	1 turn/bolt (x)	2.36
13	15	17.5	2.5	533	1 turn/bolt (x)	8.15
14	0	0	0	381	1 turn/bolt (x)	-4.76

Source: Reprinted from Gerbo et al. (2018), ©ASCE.

TABLE 2. Parametric study connection parameters. Bolded scenario indicates benchmark case. Initial plate angles ($\gamma = \beta = 10^\circ$), member angles ($\alpha = 12.5^\circ$), and relative ply angles ($\delta = 2.5^\circ$) are constant.

Scenario	d_b (mm)	t_s (mm)	t_m (mm)	$l_1 = l_2$ (mm)	e_b (mm)
A	19.1	12.7	25.1	9.50	4.29
B	19.1	15.9	25.1	9.50	5.00
C	19.1	19.1	25.1	9.50	5.70
D	22.2	12.7	25.1	9.50	4.29
E	22.2	15.9	25.1	9.50	5.00
F	22.2	19.1	25.1	9.50	5.70
G	25.4	12.7	25.1	12.7	2.70
H	25.4	15.9	25.1	12.7	3.41
I	25.4	19.1	25.1	12.7	4.11
J	19.1	12.7	19.6	12.7	3.05
K	19.1	12.7	14.2	12.7	1.87

611 **List of Figures**

612 1 Adjustable bolted steel plate connection: (A) elevation view of initial un-tightened
613 connection; (B) elevation view of final tightened connection (adapted from Gerbo
614 et al. 2019); (C) 3D view of the final tightened connection; (D) plan view of fi-
615 nal tightened connection; (E) experimental test setup; (F) bolt-tightening tools
616 (reprinted from Gerbo et al. 2018, ©ASCE.) 30

617 2 Geometric parameters: (A) untightened state (exaggerated); (B) flat plates; (C) bolt
618 eccentricity; (D) example deformation of scenario with positive δ ; (E) example
619 deformation of scenario with negative δ . [Adapted (a and b) from Gerbo et al.
620 2018, ©ASCE.] 31

621 3 Scenario 1: Longitudinal bolt surface strains (ϵ_y). 32

622 4 FE model showing (A) boundary conditions for symmetry; (B) boundary condi-
623 tions for rigid member. 33

624 5 Effect of bolt-tightening procedure: Measured and predicted curvature (ϕ) along
625 bolt axis for Scenarios 1, 2, 4, and 5. 34

626 6 Effect of amount and direction of plate bending: Measured and predicted curvature
627 (ϕ) along bolt axis for Scenarios 1, 6, 7 and 8. 35

628 7 FE predictions of maximum magnitude of curvature (ϕ) for experimentally tested
629 scenarios. 36

630 8 Effect of plate angle: Measured and predicted curvature (ϕ) along bolt axis Sce-
631 narios 9, 10, 11, 12 and 13. 37

632 9 Longitudinal lines for data identification. Numbers indicate bolt identification.
633 (Reprinted from Gerbo et al. 2018, ©ASCE.) 38

634 10 Scenario 6: Circumferential plate surface strains (ϵ_x). (Data from Gerbo et al.
635 2018, ©ASCE.) 39

636	11	Varying amount and direction of bend: measured DIC circumferential surface strain (ϵ_x) and FE predictions along lines A-D (Figure 9) for Scenarios 1, 6, 7, and 8 (Table 1). (Data from Gerbo et al. 2018, ©ASCE.)	40
637			
638			
639	12	Effect of plate thickness and bolt diameter: Predicted longitudinal bolt surface strains (ϵ_y). Letters indicate Scenario.	41
640			
641	13	FE predictions of maximum magnitude of curvature (ϕ) for parametric scenarios.	42
642	14	Effect of varying bolt diameter (d_b) and plate thickness (t_s): Predicted plate field bending and cumulative circumferential surface strains (ϵ_x) for Scenarios A-I (Table 2).	43
643			
644			
645	15	Effect of varying member flange thickness (t_m): Predicted longitudinal bolt surface strains (ϵ_y). Letters indicate Scenario.	44
646			
647	16	Predicted local peak circumferential strain (ϵ_x) in the plates near the bolt holes with varying bolt deformation(e_b).	45
648			

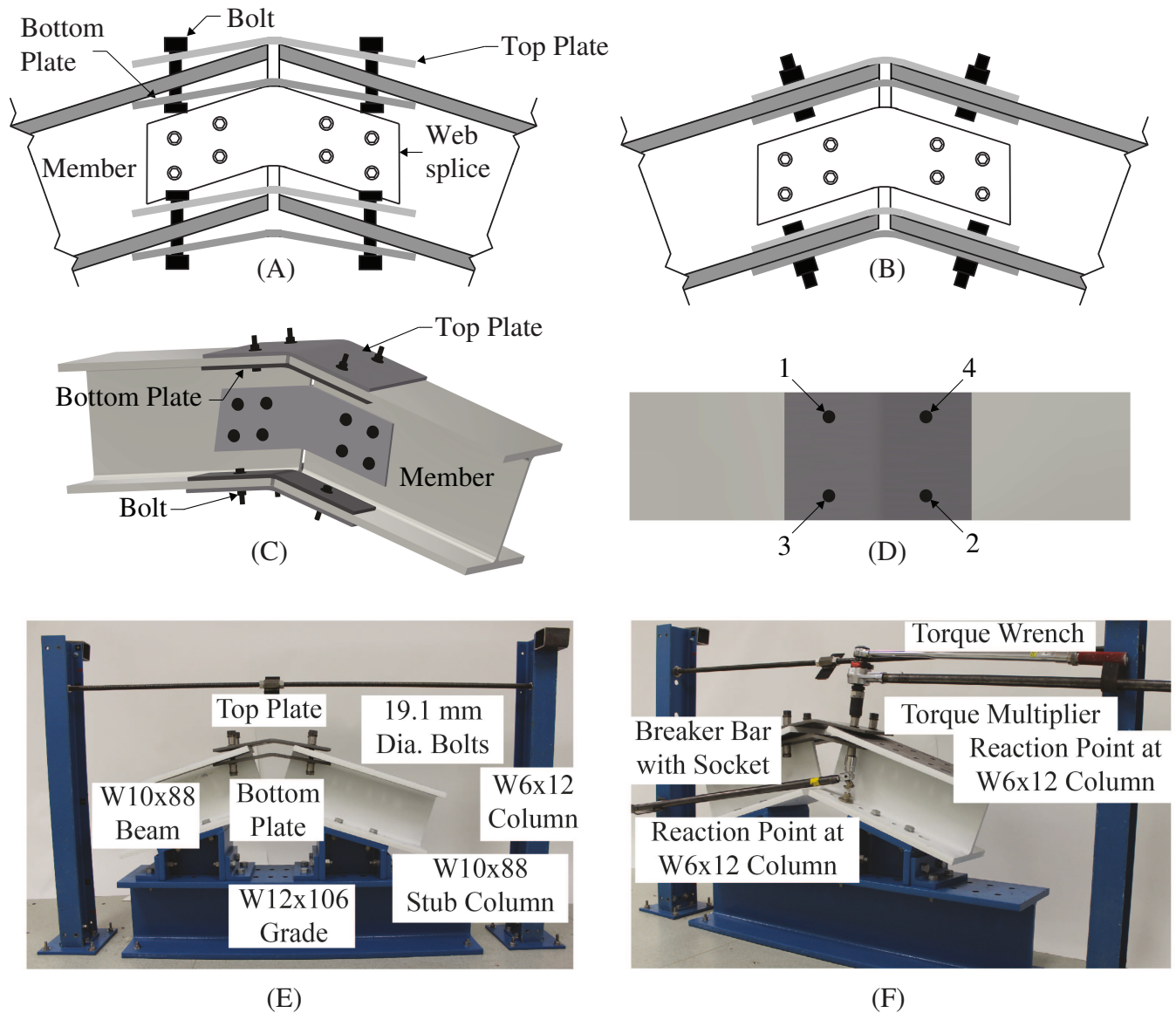


FIG. 1. Adjustable bolted steel plate connection: (A) elevation view of initial un-tightened connection; (B) elevation view of final tightened connection (adapted from Gerbo et al. 2019); (C) 3D view of the final tightened connection; (D) plan view of final tightened connection; (E) experimental test setup; (F) bolt-tightening tools (reprinted from Gerbo et al. 2018, ©ASCE.)

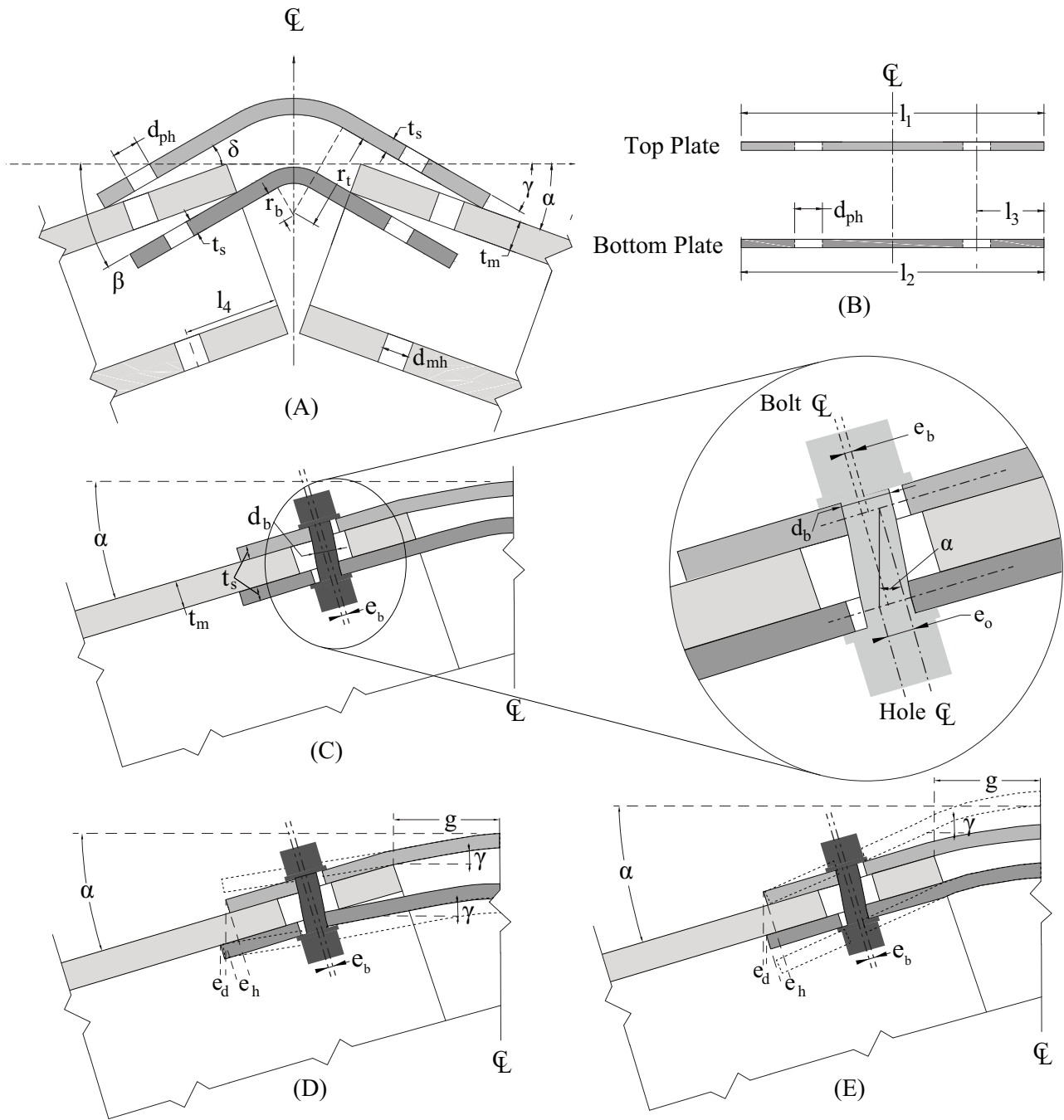


FIG. 2. Geometric parameters: (A) untightened state (exaggerated); (B) flat plates; (C) bolt eccentricity; (D) example deformation of scenario with positive δ ; (E) example deformation of scenario with negative δ . [Adapted (a and b) from Gerbo et al. 2018, ©ASCE.]

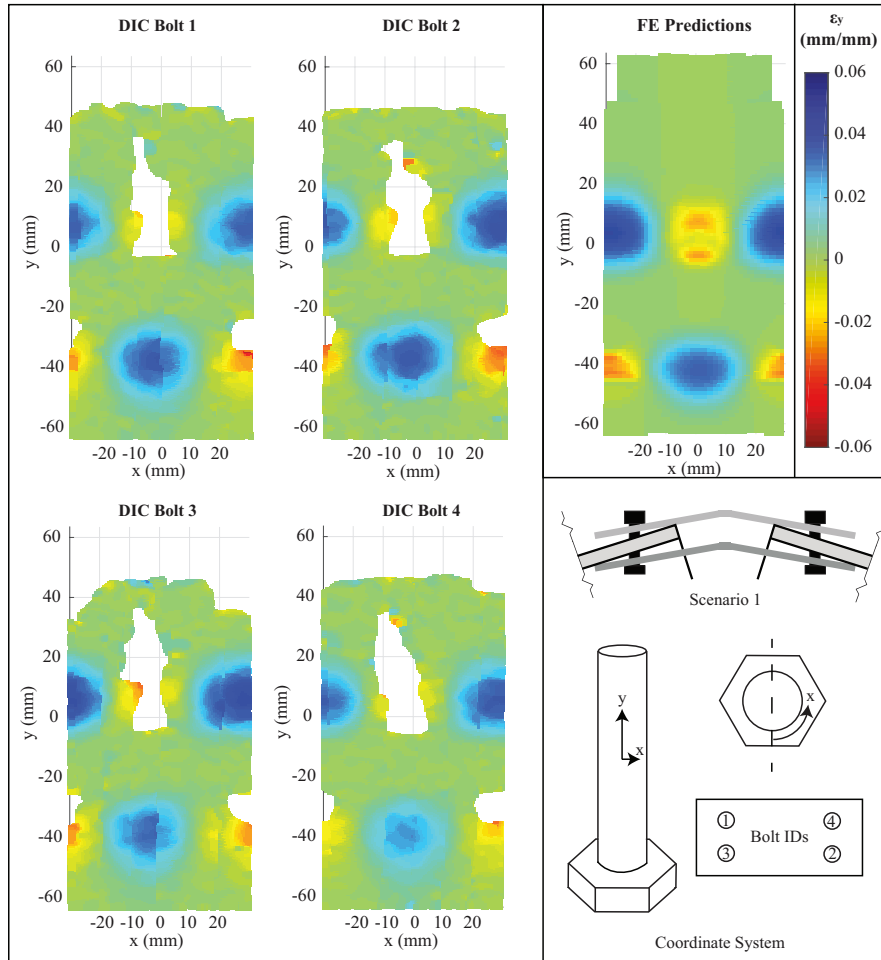
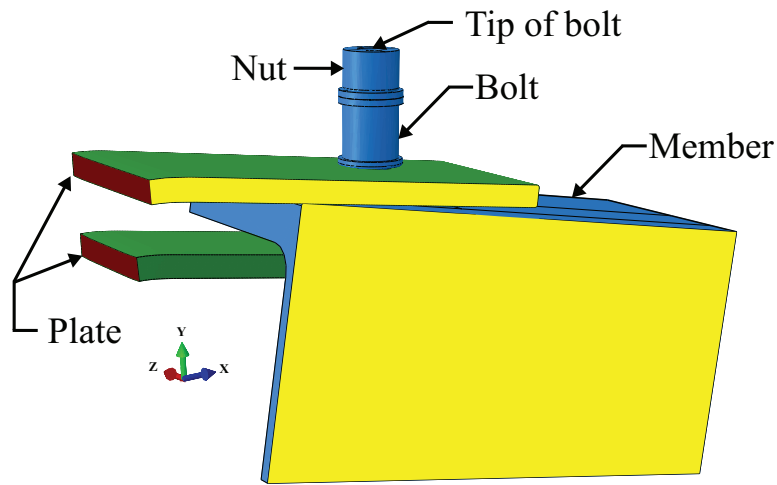
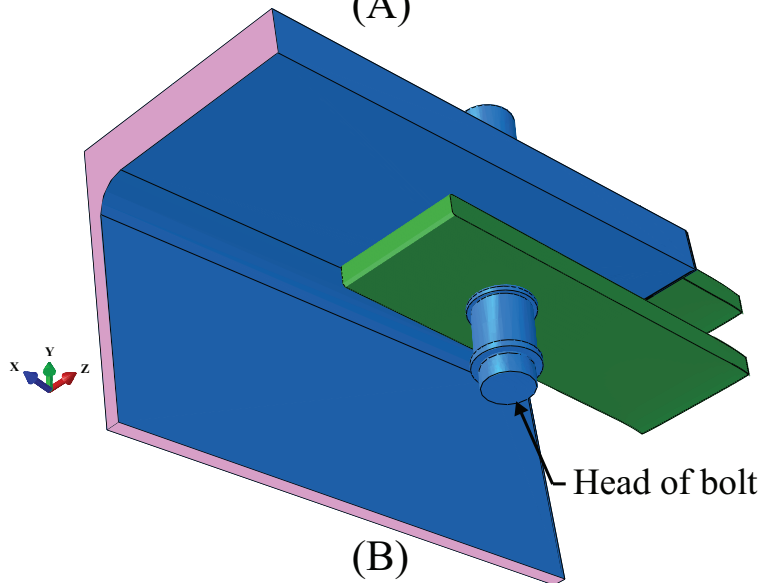


FIG. 3. Scenario 1: Longitudinal bolt surface strains (ϵ_y).



(A)



(B)

- Restrained in z direction
- Restrained in x direction
- Restrained in x, y, and z directions
- Free surfaces of plates
- Free surfaces of bolts, and member

FIG. 4. FE model showing (A) boundary conditions for symmetry; (B) boundary conditions for rigid member.

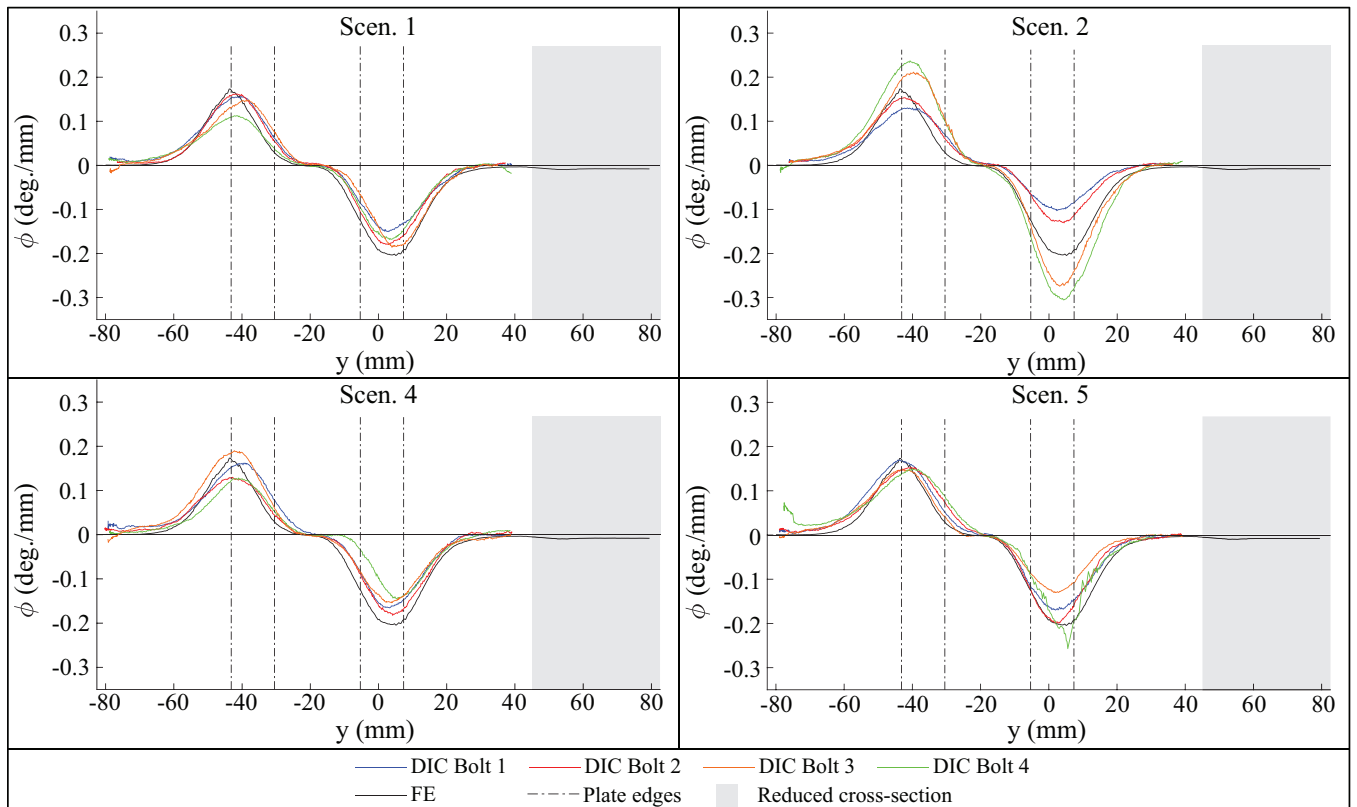


FIG. 5. Effect of bolt-tightening procedure: Measured and predicted curvature (ϕ) along bolt axis for Scenarios 1, 2, 4, and 5.

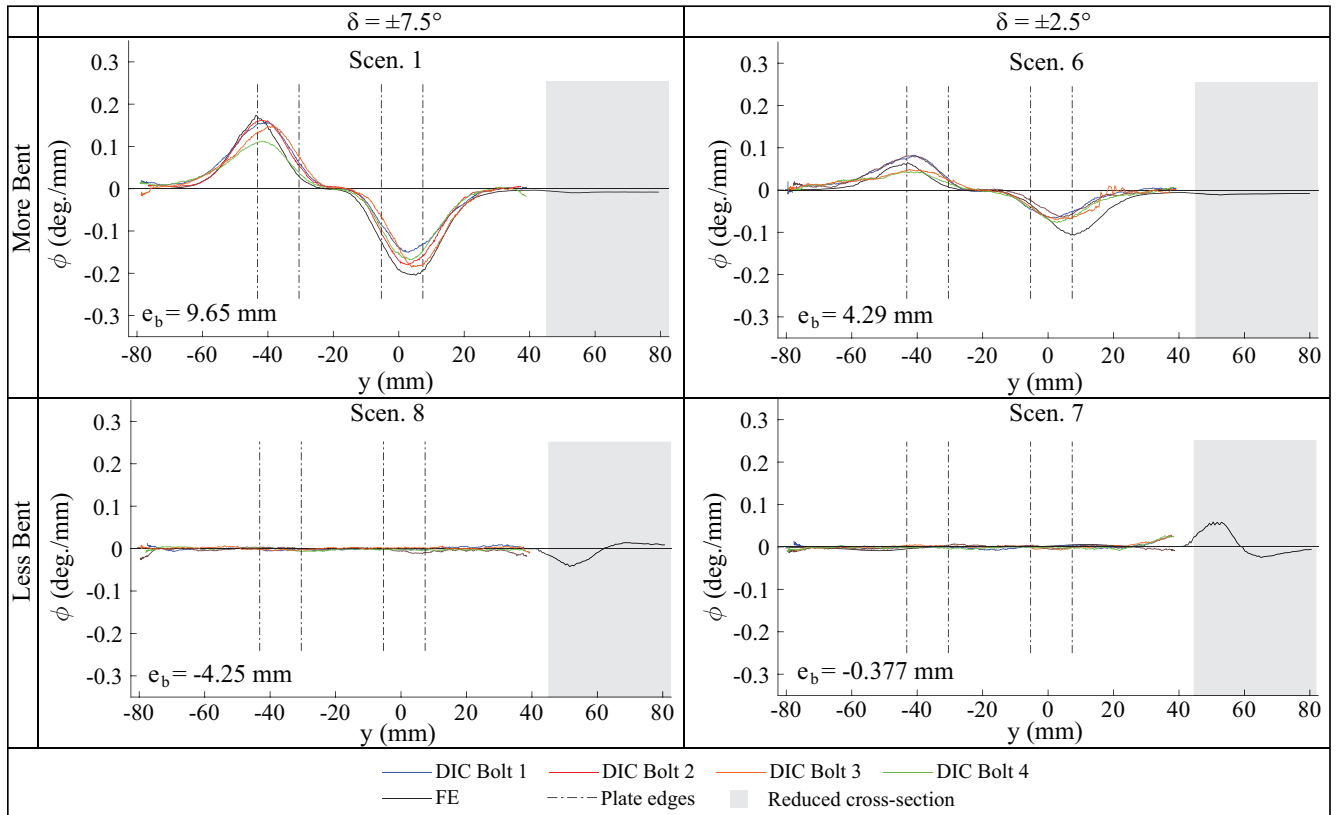


FIG. 6. Effect of amount and direction of plate bending: Measured and predicted curvature (ϕ) along bolt axis for Scenarios 1, 6, 7 and 8.

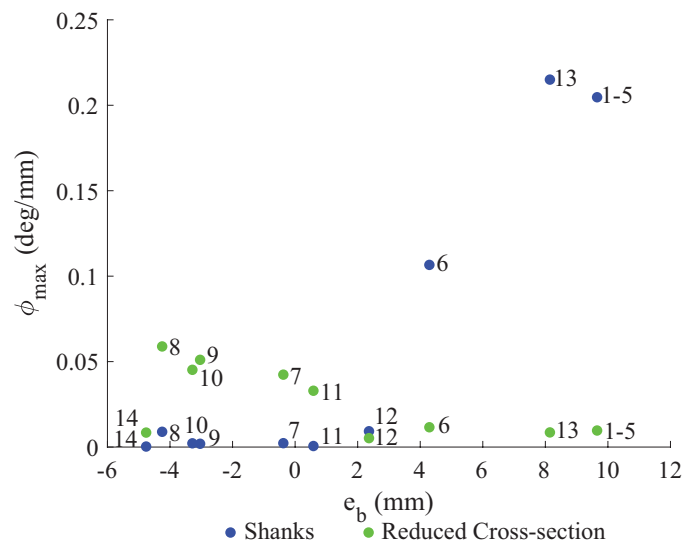


FIG. 7. FE predictions of maximum magnitude of curvature (ϕ) for experimentally tested scenarios.

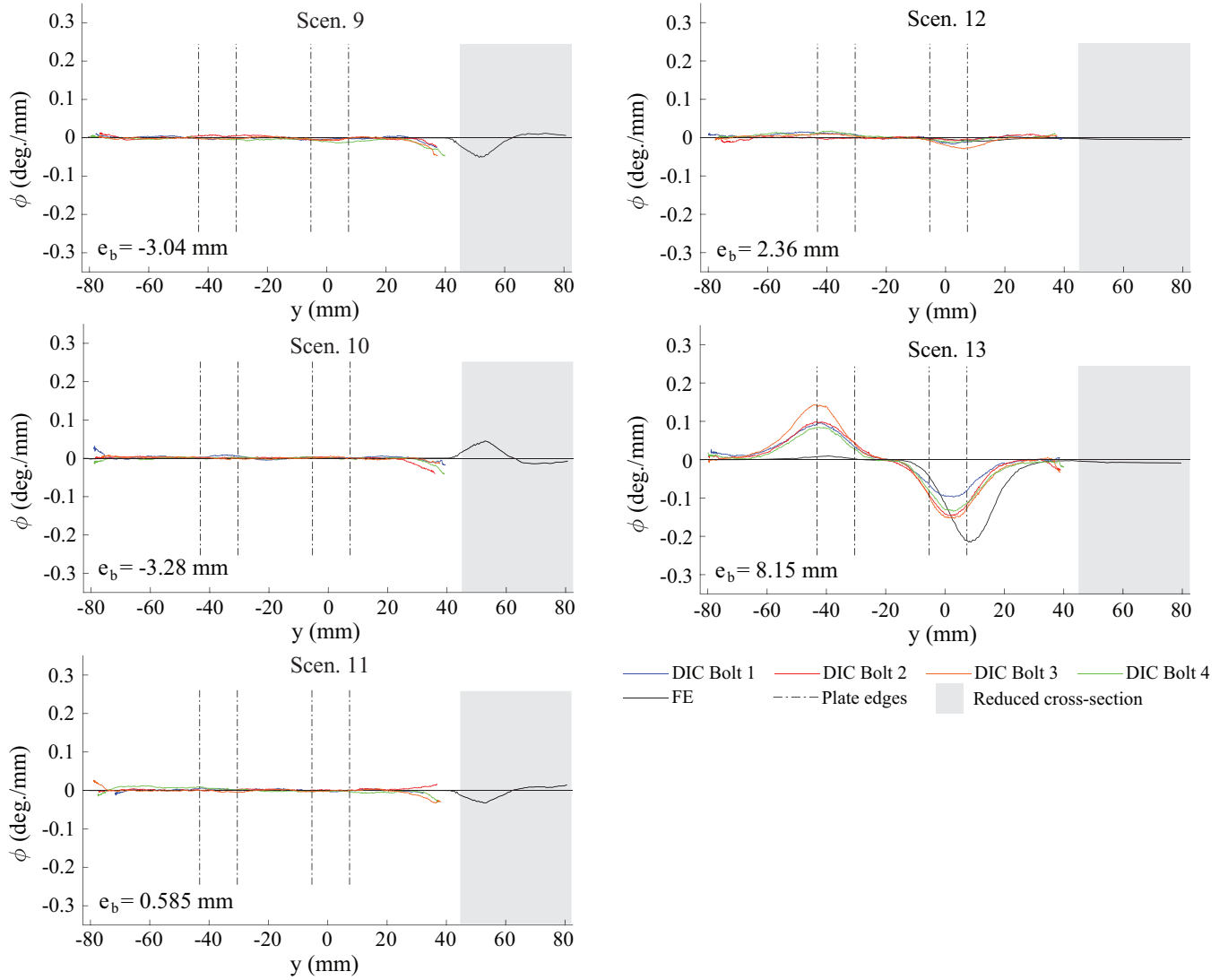


FIG. 8. Effect of plate angle: Measured and predicted curvature (ϕ) along bolt axis Scenarios 9, 10, 11, 12 and 13.

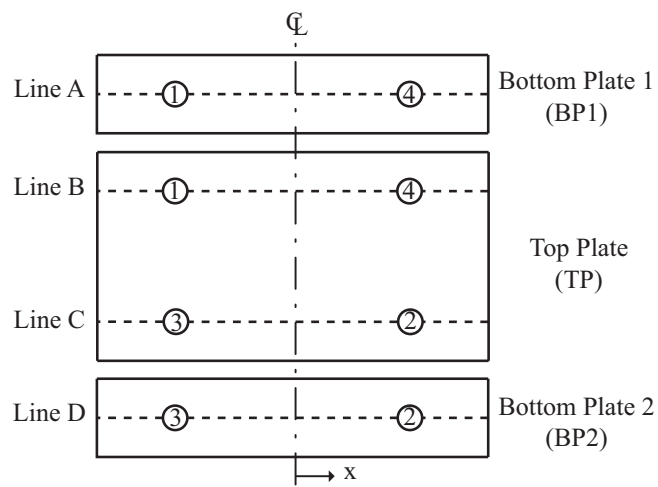


FIG. 9. Longitudinal lines for data identification. Numbers indicate bolt identification. (Reprinted from Gerbo et al. 2018, ©ASCE.)

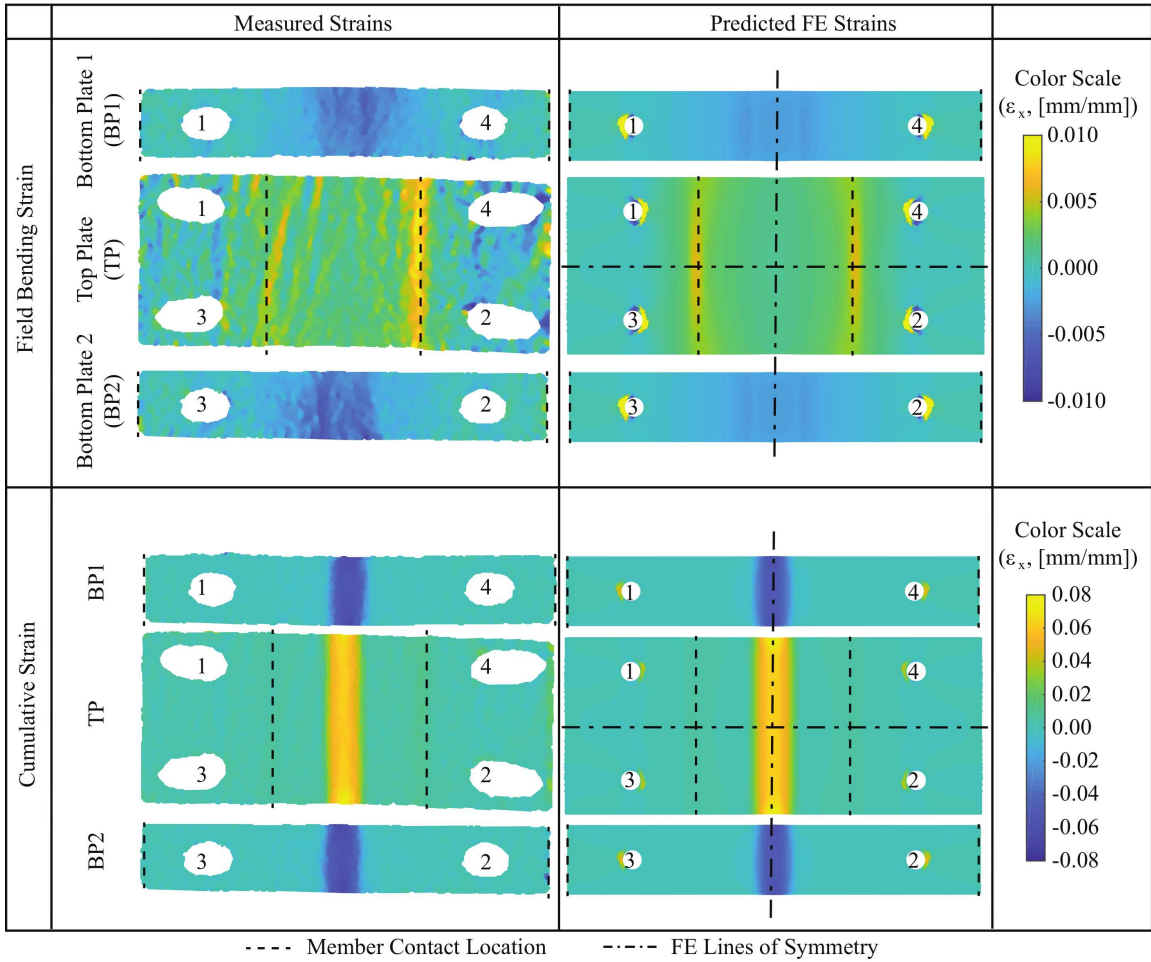


FIG. 10. Scenario 6: Circumferential plate surface strains (ϵ_x). (Data from Gerbo et al. 2018, ©ASCE.)

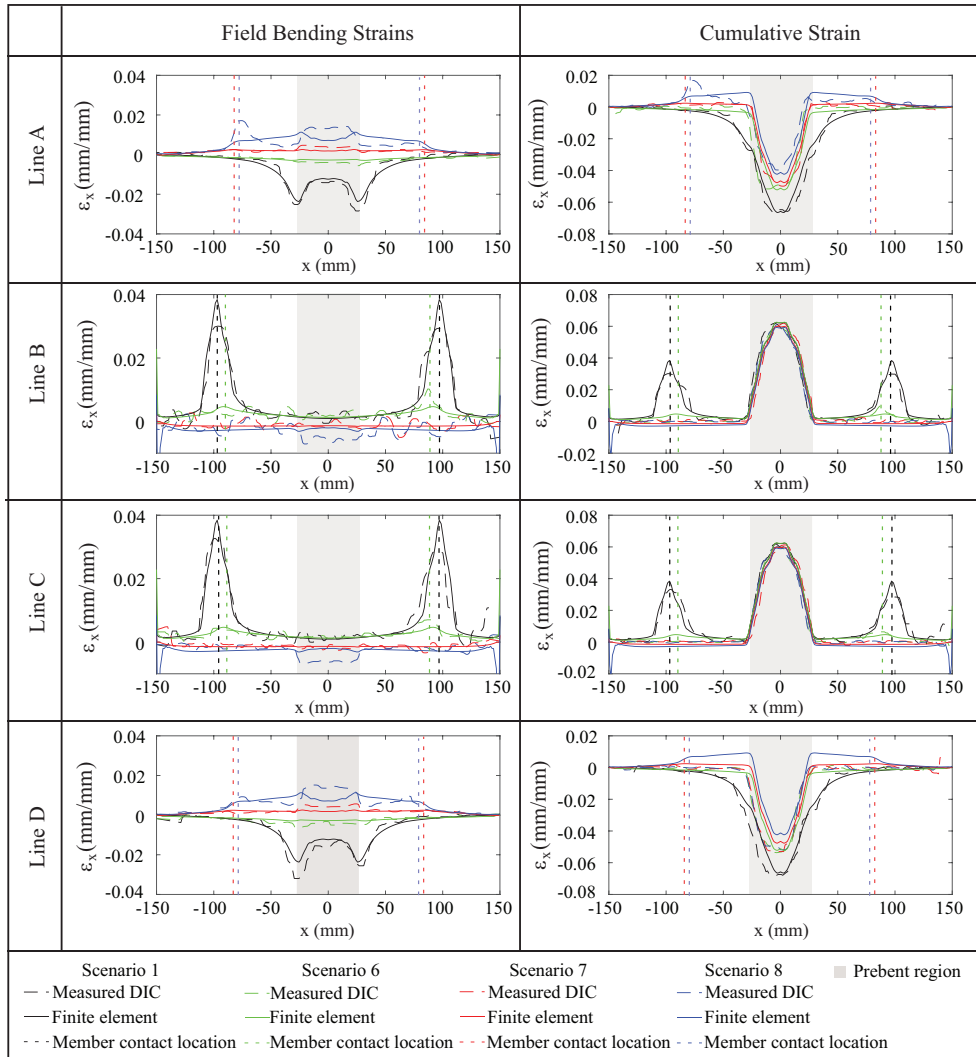
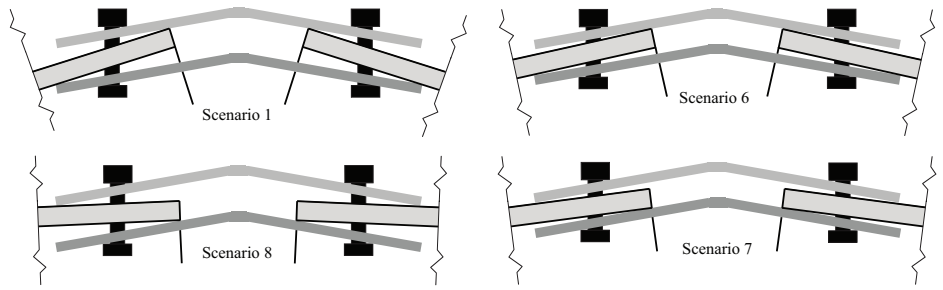


FIG. 11. Varying amount and direction of bend: measured DIC circumferential surface strain (ϵ_x) and FE predictions along lines A-D (Figure 9) for Scenarios 1, 6, 7, and 8 (Table 1). (Data from Gerbo et al. 2018, ©ASCE.)

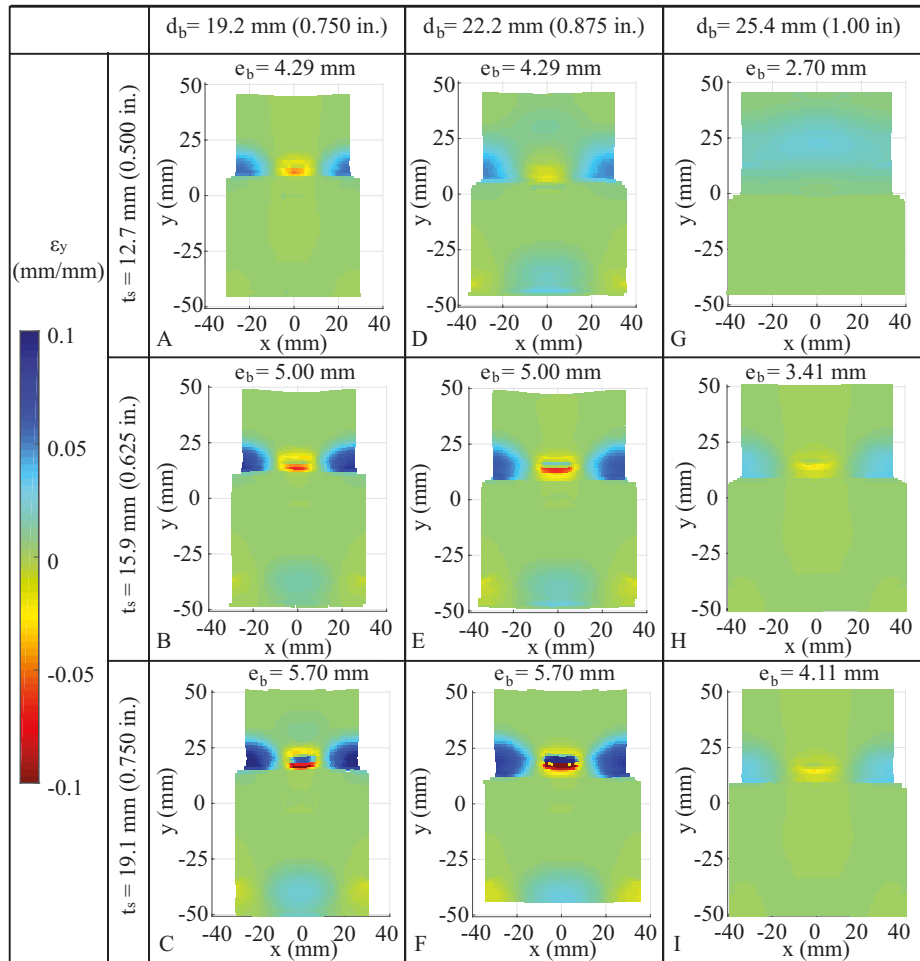


FIG. 12. Effect of plate thickness and bolt diameter: Predicted longitudinal bolt surface strains (ϵ_y). Letters indicate Scenario.

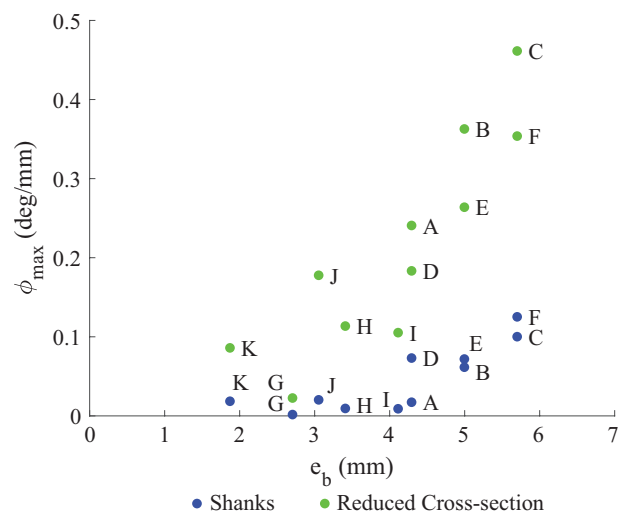


FIG. 13. FE predictions of maximum magnitude of curvature (ϕ) for parametric scenarios.

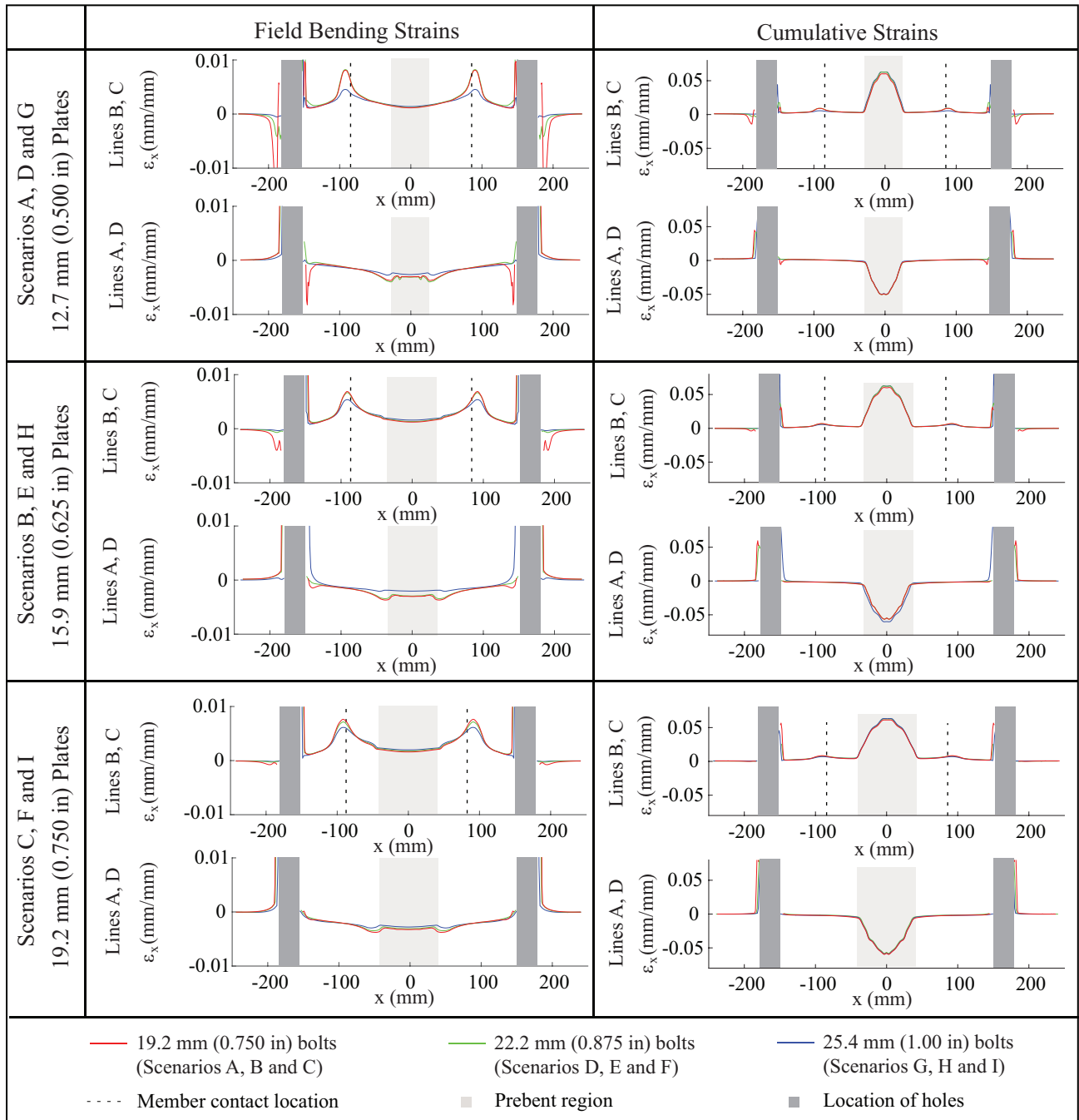


FIG. 14. Effect of varying bolt diameter (d_b) and plate thickness (t_s): Predicted plate field bending and cumulative circumferential surface strains (ϵ_x) for Scenarios A-I (Table 2).

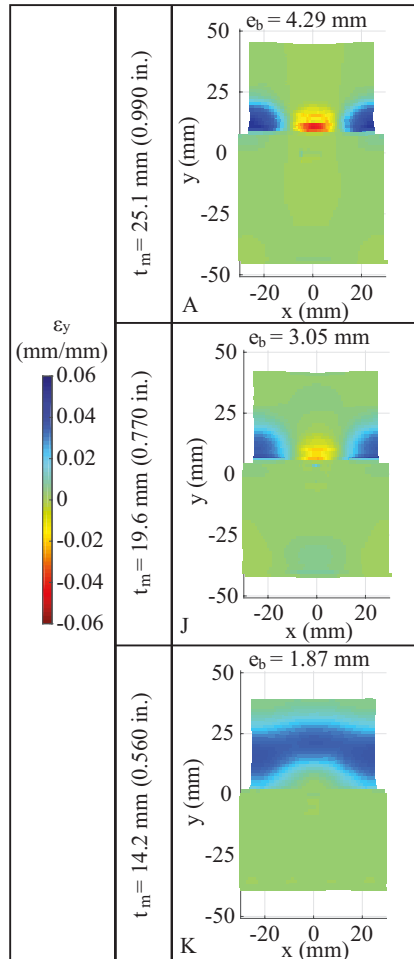


FIG. 15. Effect of varying member flange thickness (t_m): Predicted longitudinal bolt surface strains (ϵ_y). Letters indicate Scenario.

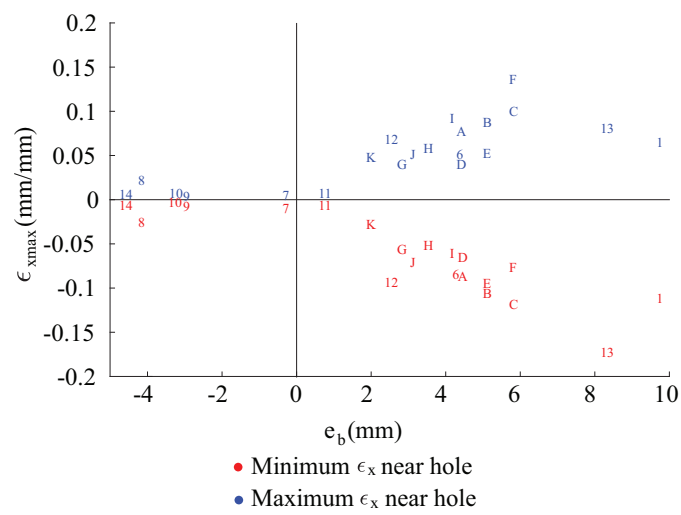


FIG. 16. Predicted local peak circumferential strain (ϵ_x) in the plates near the bolt holes with varying bolt deformation (e_b).